Journal Pre-proof

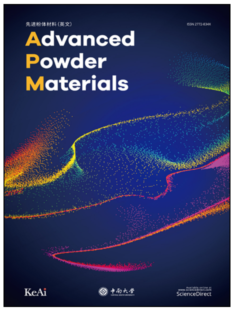

Coupling *Enteromorpha prolifera*-derived N-doped biochar with Cu-Mo_2C clusters for selective CO_2 hydrogenation to CO

Xueyuan Pan, Caikang Wang, Bei Li, Mingzhe Ma, Hao Sun, Guowu Zhan, Kui Wang, Mengmeng Fan, Linfei Ding, Gengtao Fu, Kang Sun, Jianchun Jiang

PII: S2772-834X(24)00090-3

DOI: https://doi.org/10.1016/j.apmate.2024.100259

Reference: APMATE 100259

To appear in: *Advanced Powder Materials*

Received Date: 20 October 2024

Revised Date: 19 November 2024

Accepted Date: 27 November 2024

Please cite this article as: X. Pan, C. Wang, B. Li, M. Ma, H. Sun, G. Zhan, K. Wang, M. Fan, L. Ding, G. Fu, K. Sun, J. Jiang, Coupling *Enteromorpha prolifera*-derived N-doped biochar with Cu-Mo_2C clusters for selective CO_2 hydrogenation to CO, *Advanced Powder Materials*, https://doi.org/10.1016/j.apmate.2024.100259.

This is a PDF file of an article that has undergone enhancements after acceptance, such as the addition of a cover page and metadata, and formatting for readability, but it is not yet the definitive version of record. This version will undergo additional copyediting, typesetting and review before it is published in its final form, but we are providing this version to give early visibility of the article. Please note that, during the production process, errors may be discovered which could affect the content, and all legal disclaimers that apply to the journal pertain.

© 2024 Central South University. Publishing services by Elsevier B.V. on behalf of KeAi Communications Co. Ltd.

Journal Pre-proof

Coupling *Enteromorpha prolifera*-derived N-doped biochar with Cu-Mo_2C clusters for selective CO_2 hydrogenation to CO

Xueyuan Pan[a, 1], Caikang Wang[a, b, 1], Bei Li[a], Mingzhe Ma[a], Hao Sun[a,*], Guowu Zhan[c,*], Kui Wang[a, d], Mengmeng Fan[d], Linfei Ding[d], Gengtao Fu[b,*], Kang Sun[a], Jianchun Jiang[a]

[a] Key Laboratory of Biomass Energy and Material, Jiangsu Province, Key and Open Laboratory of Forest Chemical Engineering, SFA, National Engineering Laboratory for Biomass Chemical Utilization, Institute of Chemical Industry of Forest Products, Chinese Academy of Forestry, Nanjing 210042, China

[b] Jiangsu Key Laboratory of New Power Batteries, Jiangsu Collaborative Innovation Center of Biomedical Functional Materials, School of Chemistry and Materials Science, Nanjing Normal University, Nanjing 210023, China

[c] Academy of Advanced Carbon Conversion Technology, College of Chemical Engineering, Huaqiao University, Xiamen, Fujian, 361021, China

[d] Co-Innovation Center of Efficient Processing and Utilization of Forest Resources, Nanjing Forestry University, Nanjing 210042, China

* Corresponding authors. E-mail addresses: sunhao@icifp.cn (H. Sun); gwzhan@hqu.edu.cn (G. Zhan); gengtaofu@njnu.edu.cn (G. Fu)

[1] These authors contributed equally to this work.

Journal Pre-proof

Acknowledgments

The authors are grateful for the financial support from National Natural Science Foundation of China (32101474 and 42377249) and National Key Research and Development Program of China (2023YFD2201605). The work was supported from the National and Local Joint Engineering Research Center of Biomedical Functional Materials and a project sponsored by the Priority Academic Program Development of Jiangsu Higher Education Institutions.

Journal Pre-proof

Photograph and biography of Authors

Xueyuan Pan is currently a Ph.D. candidate in the major of biomass energy and materials at the Institute of Chemical Industry of Forest Products, under the supervision of Prof. Jianchun Jiang. Her research is focused on the design of carbon-based catalysts for CO_2 hydrogenation.

Hao Sun received his Ph.D. degree at the School of Chemistry and Materials Science at Nanjing Normal University in 2017. He is currently an Associate researcher at Institute of Chemical Industry of Forest Products, Chinese Academy of Forestry. His major research interests are focused on the biochar-based materials for energy catalysis. He has presided over the national natural science foundation projects, national key research and development plan sub-task and so on. He has been recognized with five provincial-level awards.

Guowu Zhan received his B.Eng. and M.Eng. in Chemical Engineering from Xiamen University (China) in 2009 and 2012, respectively. He obtained his Ph.D. degree in 2016 at the National University of Singapore (NUS). Following postdoctoral work at the NUS, he joined the faculty at Huaqiao University (China) as a Distinguished Professor of Minjiang Scholars in 2018. He has published more than 130 research papers in well-reputed journals. Currently, his major research interests are focused on the design and fabrication of integrated nanocatalysts for CO2 hydrogenation.

Journal Pre-proof

Journal Pre-proof

Gengtao Fu received his Ph.D. degree at the School of Chemistry and Materials Science at Nanjing Normal University in 2017. He spent one year (2015–2016) as a visiting scholar at the University of Texas at Austin. He was a research fellow at Nanyang Technological University working with Prof. Jong-Min Lee (2017–2019). Then he worked at the University of Texas at Austin with Prof. John B. Goodenough (2019–2021). He is currently a full professor at College of Chemistry and Materials Science at Nanjing Normal University. His expertise and research interests are mainly focused on rare-earth-based electrocatalytic materials for efficient energy conversion.

Jianchun Jiang, a distinguished member of the Chinese Academy of Engineering, is a renowned scientist in the field of forest chemical engineering. His contributions include the development of advanced manufacturing techniques for high-value products, which have not only broken foreign monopolies but have also found widespread application in 15 provinces and have been exported to over 10 countries. Dr. Jiang has been recognized with four National Science and Technology Progress Awards and ten provincial-level awards for his outstanding contributions. His scholarly output includes over 400 published papers, and he holds more than 70 authorized patents. His research has played a pivotal role in elevating China's capabilities in the field of forest chemical engineering, fostering substantial growth in the industry. Dr. Jiang stands as a prominent figure and exemplary representative in China's forest chemical engineering sector.

Journal Pre-proof

Graphical Abstract

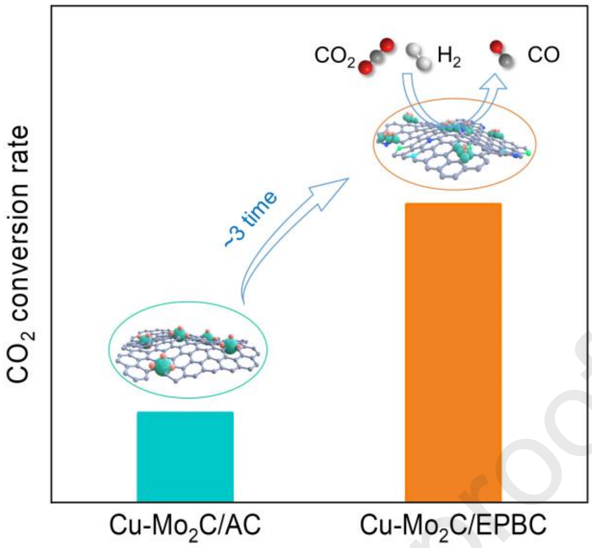

N-doped biochar supported Cu-Mo_2C cluster (Cu-Mo_2C/EPBC) was constructed via an *Enteromorpha prolifera*-derived strategy. Unlike traditional Cu-Mo_2C/AC (activated carbon), Cu-Mo_2C/EPBC presents the better graphitization degree and larger specific surface area, while can firmly anchors Cu-Mo_2C clusters due to riched pyridine-N. Cu-Mo_2C/EPBC shows an improved CO selectivity of 99.95% at 500 °C compared with Cu-Mo_2C/AC (99.60%), and about 3-fold CO_2 conversation rate.

Journal Pre-proof

Coupling *Enteromorpha prolifera*-derived N-doped biochar with Cu-Mo_2C clusters for selective CO_2 hydrogenation to CO

Journal Pre-proof

Abstract: CO_2 conversion to CO *via* the reverse water-gas shift (RWGS) reaction is limited by a low CO_2 conversion rate and CO selectivity. Herein, an efficient RWGS catalyst is constructed through *Enteromorpha prolifera* derived N-rich mesoporous biochar (EPBC) supported atomic-level Cu-Mo_2C clusters (Cu-Mo_2C/EPBC). Unlike traditional activated carbon (AC) supported Cu-Mo_2C particles (Cu-Mo_2C/AC), the Cu-Mo_2C/EPBC not only presents the better graphitization degree and larger specific surface area, but also uniformly and firmly anchors atomic-level Cu-Mo_2C clusters due to the existence of pyridine nitrogen. Furthermore, the pyridine N of Cu-Mo_2C/EPBC strengthens an unblocked electron transfer between Mo_2C and Cu clusters, as verified by X-ray absorption spectroscopy. As a result, the synergistic effect between pyridinic N anchoring and the clusters interaction in Cu-Mo_2C/EPBC facilitates an improved CO selectivity of 99.95% at 500 °C compared with traditional Cu-Mo_2C/AC (99.60%), as well as about 3-fold CO_2 conversion rate. Density functional theory (DFT) calculations confirm that pyridine N-modified carbon activates the local electronic redistribution at Cu-Mo_2C clusters, which contributes to the decreased energy barrier of the transition state of CO*+O*+2H*, thereby triggering the transformation of rate-limited step during the redox pathway. This biomass-derived strategy opens perspective on producing sustainable fuels and building blocks through the RWGS reaction.

Keywords: *Enteromorpha prolifera*; N-doped biochar; Cu-Mo_2C clusters; Electronic interaction; CO_2 hydrogenation

Journal Pre-proof

1. Introduction

The ecological and environmental issues associated with CO_2 emission from fossil fuels are driving the discovery and implementation of renewable and sustainable energy technologies [1-4]. One promising conversion route is the catalytic hydrogenation of CO_2 using a renewable energy-based "green hydrogen" source. Controlling the conversion rate, selectivity and stability of reverse water gas shift (RWGS) reaction for CO production or syngas (H_2 + CO) is regarded as one of the most promising reactions to mitigate the further rise of atmospheric CO_2 levels but remains a great challenge owing to low reaction kinetics [5-8].

Until now, the Cu-Mo_2C catalysts with fabricated Cu^+ sites exhibit higher catalytic activity and stability for the RWGS compared with other metal-based catalysts [9-13], owing to the strong interaction between Cu and β-Mo_2C. The Mo_2C support not only promotes the dispersion and prevents aggregation of Cu^+ sites, but also assists the hydrogen dissociation and C=O bond scissoring [1, 14, 15]. However, the contribution of atomic Mo_2C with modified electronic structure to the Cu sites and RWGS performance was rarely studied. It is demonstrated that N-doped carbon could act as a carbon support for highly dispersed formation of Mo_2C with flexible electron modulation through the strong metal-support interaction (SMSI) effect [16-22], while the traditional preparation of carbon supports with mesopores and N-functional groups requires complicated procedures and large amounts of additional nitrogenous reagents [10, 23, 24]. It is interesting that the utilization of nitrogenous biomass to prepare N-doped carbon appears as a promising approach without the introduction of nitrogen sources [25]. The *Enteromorpha prolifera* (EP) is an alga containing abundant cellulose and protein, which are excellent raw materials candidates for synthesis of N-doped mesopore carbon. Meanwhile, the excess EP in the ocean has been causing the green tide and inducing severe ecological damage and huge economic loss around the world, and there are more than 1 million tons/year of EP need dispose of in China.

Herein, the EP derived biochar (EPBC) with abundant pyridine N and mesoporous structure was prepared as the support to anchor atomic-level Cu-Mo_2C clusters. The enhancement of the SMSI effect between EPBC and β-Mo_2C induced by nitrogen anchoring facilitates the formation of abundant Mo_2C clusters with electron-deficient states, thus leading to the subsequent atomic-level Cu-Mo_2C clusters interface on the surface of EPBC. X-ray photoelectron spectroscopy (XPS) and X-ray absorption spectroscopy (XAS) verified the nitrogen anchoring effect and a stronger electronic interaction and unblocked electron transfer between Mo_2C and Cu clusters in Cu-Mo_2C/EPBC. Those effects were not observed for activated carbon supported Cu-Mo_2C particles (Cu-Mo_2C/AC). The constructed Cu-Mo_2C/EPBC exhibits an improved CO selectivity of 99.95% at 500 °C compared with traditional Cu-Mo_2C/AC catalyst (99.60%), as well as about 3-fold CO_2 conversion rate. Density functional theory

Journal Pre-proof

(DFT) calculations demonstrate that the modification of nitrogen can significantly alter the rate-limit step and decrease the energy barrier of intermediate, and accordingly boost the catalytic performance of Cu-Mo_2C/EPBC in CO synthesis.

2. Results and discussion

2.1. Preparation and characterization of Cu-Mo_2C/EPBC

Fig. 1 demonstrates the synthesis evolution of Cu-Mo_2C/EPBC derived from the EP. Specifically, the EPBC was first prepared via a simple carbonization process under N_2 atmosphere at pre-carbonization temperatures of 800 °C. The impregnation method was then used to anchor the Cu and Mo species, and further calcined under H_2/N_2 atmosphere to obtain the Cu-Mo_2C/EPBC-800 catalyst. If not otherwise specified, the Cu-Mo_2C/EPBC-800 was denoted as Cu-Mo_2C/EPBC. For comparison, the traditional activated carbon without N functional groups was also selected as carrier to load Cu-Mo_2C sites. To investigate the properties of EPBC, a series of experiments were conducted including X-ray diffraction (XRD), Raman spectra and N_2 adsorption-desorption isotherms. XRD pattern of EPBC (Fig. S1a) shows the diffraction peak of graphitized carbon [26, 27]. A lower I_D/I_G ratio was observed in EPBC than that of traditional AC (Fig. S1b), suggesting a larger average size of the sp^2 carbon structural domain, indicative of improved graphitization degree [28, 29]. With respect to traditional AC support, the EPBC shows a typical type IV isotherm with H4 hysteresis loop and an increase in mesopore volume, indicating a potential structure advantage in EPBC (Fig. S2). As illustrated by N 1s XPS spectra (Fig. S3), the EPBC has sufficient N-functional groups, which is favored to the dispersion of Cu-Mo_2C sites. The corresponding various nitrogen content were summarized in Table S2. As a comparison, EPBC at different pre-carbonization temperatures (850 °C and 900 °C) were also prepared and corresponding structure feature were detected (Fig. S4-6, Table S1-2). These EPBCs exhibit similar mesoporous structure and graphitization degree, while the EPBC-800 presents the highest total N, pyridinic N and pyrrolic N contents.

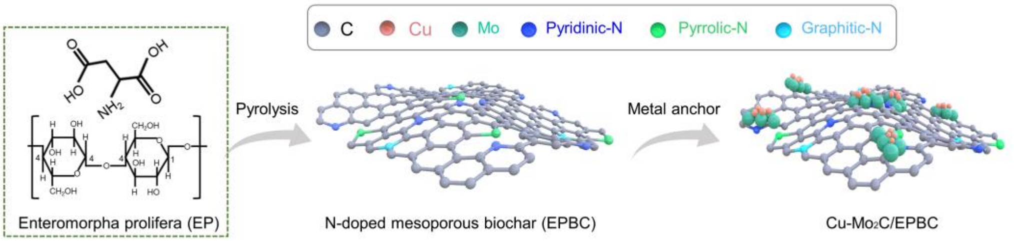

Fig. 1. Schematic illustration of the synthesis evolution from EPBC to Cu-Mo_2C/EPBC.

We utilized the aberration-corrected transmission electron microscopy (AC-TEM) to reveal the fine atomic-scale structure of the Cu-Mo_2C/EPBC catalyst. As depicted in Fig. 2a-b, the Aberration-

Journal Pre-proof

corrected high-angle annular dark-field scanning transmission electron microscopy (HAADF-STEM) images show uniformly distributed bright spots on the Cu-Mo_2C/EPBC, which correspond to the presence of nanocluster and do not agglomerate into large particles. Linear energy-dispersive spectra (EDS) results show that the clusters are Mo atoms (Fig. 2c), and the lattice spacings of 0.26 and 0.23 nm are respectively ascribed to the (100) and (101) planes in the β-Mo_2C (Fig. 2d), which reveals the Mo_2C clusters formation on the surface of EPBC. However, the Cu sites is hardly discerned owing to its low concentration. To clarify the Cu site tend to be more dispersed on the surface of Mo_2C clusters rather than EPBC, Cu/EPBC with equivalent Cu species was prepared and investigated. It is notable that Cu species are aggregated into larger Cu particle in the absence of Mo_2C species (Fig. S7a-c). This reveals the atomic-level Cu sites of Cu-Mo_2C/EPBC are anchored on the surface of Mo_2C clusters. DFT calculations were further conducted to investigate the adsorption tendency of Cu clusters. The plane (100) of Mo_2C, pyridinic-N and graphite carbon of EPBC were chosen as the support surface. It can be found that the representative Cu clusters with four atoms (Cu_4) exhibits the lowest value of chemisorption energy at Mo_2C with respect to other two support surface, revealing that Cu clusters tend to be more dispersed on the surface of Mo_2C clusters rather than EPBC (Fig. S7d, Table S3). Combined with the above results, it is reasonable speculated that the existence of N in EPBC matrix promotes preferential anchoring of β-Mo_2C clusters, thus leading to the subsequent high dispersion of atomic-level Cu-Mo_2C clusters on the surface of EPBC [30]. The Cu-Mo_2C bimetal on EPBC display a uniform distribution according to the result of energy-dispersive spectra (EDS) elemental mapping (Fig. 2e). The cluster size distribution of Cu-Mo_2C/EPBC presents an average particle size of 0.79 nm (Fig. 2f). Transmission electron microscopy (TEM) analysis of the other catalysts including Cu-Mo_2C/AC, Cu-Mo_2C/EPBC-850 and Cu-Mo_2C/EPBC-900 reveal the Cu-Mo_2C species in Cu-Mo_2C/AC without nitrogen doping were aggregated into large particles with average particle size of 5.31 nm (Fig. S8), indicating the synergistic effect between N anchoring and the clusters' interaction is responsible for the anchor of high disperse Cu-Mo_2C clusters [31]. The presence of noticeable metal nanoparticles for Cu-Mo_2C/AC were observed in Fig. S9a-b, in which the Mo and Cu shows more obvious particle aggregation phenomenon than that of Cu-Mo_2C/EPBC (Fig. S9c), and a distinct Mo-Cu interaction. These results confirm the synergistic effect between N anchoring and the clusters interaction accounts for the excellent dispersion of Cu-Mo_2C sites in Cu-Mo_2C/EPBC.

Journal Pre-proof

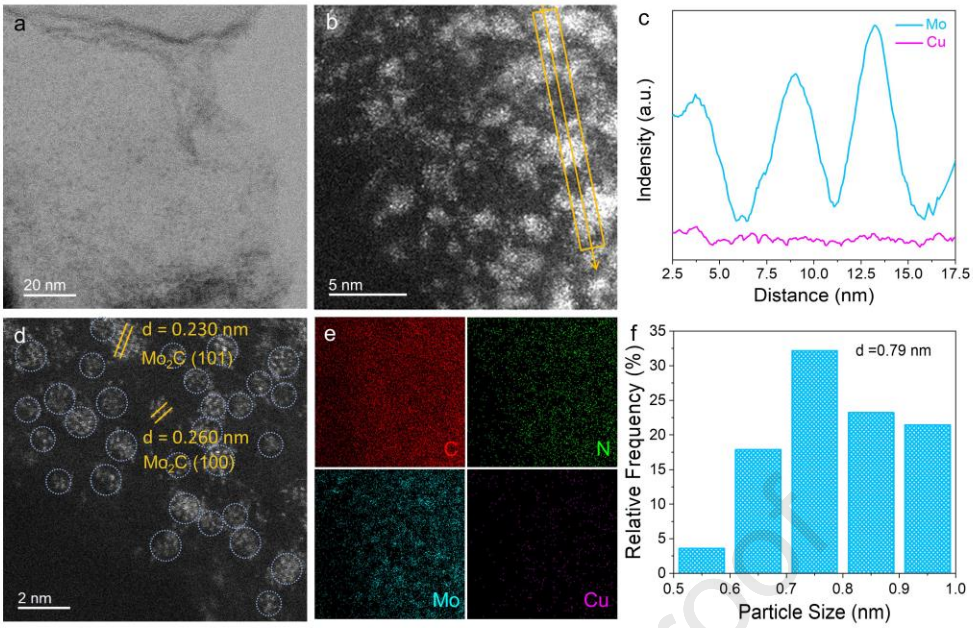

Fig. 2. The dispersed state of Cu-Mo$_2$C metal at different matrix. (a) AC TEM; (b) HAADF-STEM at 5nm; (c) Linear EDS spectra alone the yellow line in the (b); (d) HAADF-STEM at 2 nm; (e) EDS elemental mapping of Cu-Mo$_2$C/EPBC; (f) Particle size distribution from (d).

To further demonstrate the synergistic effect between pyridinic N anchoring and the clusters' interaction, the obtained Cu-Mo$_2$C/EPBC and Cu-Mo$_2$C/AC were characterized by XRD for structural determination (Fig. 3a). XRD diffraction peaks of Cu-Mo$_2$C/AC at 34.4°, 38.0°, 39.4°, 52.1°, 61.5°, 69.6°, 74.6° and 75.5° are assigned to the (100), (002), (101), (102), (110), (103), (112), and (201) plane of β-Mo$_2$C (JCPDS 35-0787), and the diffraction peaks at 2θ of 43.3° and 50.4° are ascribed to Cu [32, 33]. For Cu-Mo$_2$C/EPBC, no β-Mo$_2$C and Cu diffraction peaks were observed at Fig. 3a, indicating the atomic phase or cluster dispersion of Cu-Mo$_2$C on the EPBC surface. This phenomenon is likely attributable to the fact that the existence of pyridinic N in EPBC matrix promotes preferential anchoring of β-Mo$_2$C clusters, thus leading to the subsequent high dispersion of atomic-level Cu-Mo$_2$C clusters. C 1s XPS pattern displays that the Cu-Mo$_2$C/EPBC possesses a strong signal of C-N bonds in 286.74 eV compared with Cu-Mo$_2$C/AC (Fig. S10), verifying the absence of N-functional groups in Cu-Mo$_2$C/AC. An increase in the intensity of Mo$_2$C diffraction peak was observed in Cu-Mo$_2$C/EPBC-850 and Cu-Mo$_2$C/EPBC-900 (Fig. S11). The observation further suggests the relatively high content of pyridinic N (52.84%) in Cu-Mo$_2$C/EPBC is favored to preferential anchor abundant β-Mo$_2$C clusters [34]. This result can be supported by TEM, the N 1s XPS spectra and corresponding N proportion (Fig. S12-13 and Table S2). The Cu-Mo$_2$C/EPBC with sufficient pyridinic N anchoring and clusters interaction shows the high dispersion of Cu-Mo$_2$C clusters. Since pyridinic N-bridged metal sites are usually utilized as basic sites for CO$_2$ chemisorption through acid–base interaction, the CO$_2$

Journal Pre-proof

temperature programmed desorption (CO_2-TPD) experiments was also conducted. As expected, the Cu-Mo_2C/EPBC displays the larger α and β peak, representing the enhanced adsorption in CO_2 species in metal active sites with assistance of abundant pyridinic N [24, 26, 35] (Fig. S14 and Table S4). Compared with Cu-Mo_2C/AC, Cu-Mo_2C/EPBC possesses an obvious H4 loop curve with a larger specific surface area (S_{BET}) of 603.43 $m^2 g^{-1}$ (Fig. 3b and Table S5), a mesoporous structure distributed in the range of 2-20 nm (Fig. 3c), as well as a better graphitization degree (Fig. 3d). These excellent structure features in Cu-Mo_2C/EPBC are favored to adsorb/activate CO_2 and further switch into CO through RGWS reaction [36-38]. The high-resolution XPS spectra for the Mo 3d and Cu 2p regions were added to investigate the impact of pyridinic N on electronic structure of Mo and Cu in Cu-Mo_2C/EPBC. As depicted in Fig. 3e and 3f, the existence of pyridinic N results in positive shift in the binding energies of Mo 3d and Cu 2p XPS of Cu-Mo_2C/EPBC by 0.30 eV and 0.42 eV, respectively, due to the enhanced SMSI effect induced by pyridinic N. Such a shift promotes more electron transfer from Mo to nonmetal (C and N), and thus generating more Mo_2C clusters with electron-deficient states (Mo^{4+} and Mo^{6+}). The enhancement of SMSI effect induced by pyridinic N anchoring facilitates the Cu species absorbed on the special Mo_2C clusters with electron-deficient states, thus preventing the aggregation of Cu particles and formatting atomic-level Cu-Mo_2C clusters interface [39]. More importantly, the highly dispersed Cu species on the special Mo_2C facilitates the formation of unblocked electron transfer channel between Mo_2C and Cu clusters, where Cu species is in the electron-deficient state [40, 41]. Considering the absence of pyridinic N in AC matrix, the synergistic effect between pyridinic N anchoring and the clusters' interaction accounts for the perfect dispersion and electron transfer of Cu-Mo_2C in Cu-Mo_2C/EPBC.

Journal Pre-proof

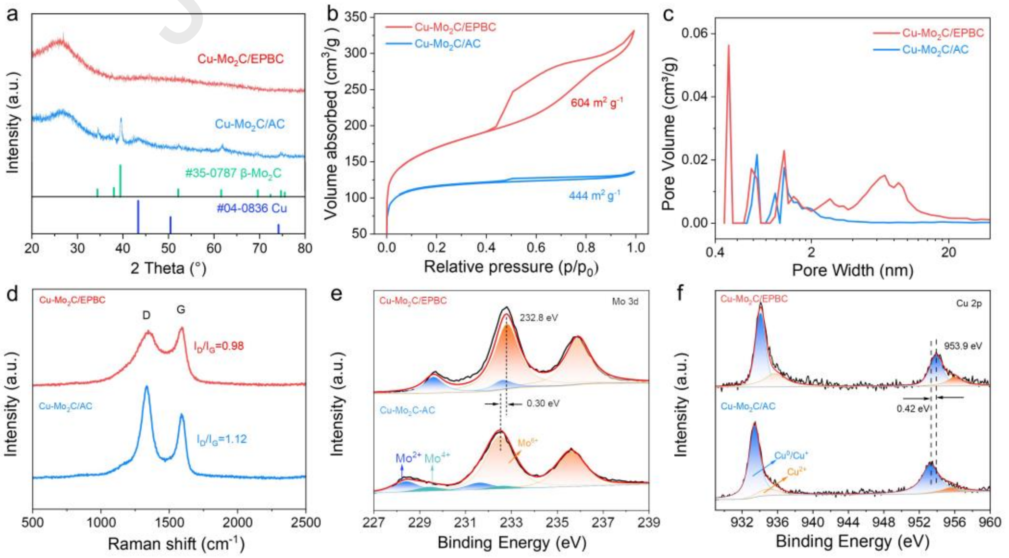

Fig. 3. The structure difference of Cu-Mo_2C metal sites loaded on EPBC and AC matrix. (a) XRD patterns; (b) N_2 adsorption-desorption isotherms; (c) pore size distributions; (d) Raman spectra; (e,f)

XPS spectra of Mo 3d (e), Cu 2p (f).

To clarify the clusters interaction between Cu and Mo_2C, XPS was applied to gain insights into the surface chemical constituent of Cu-Mo_2C/EPBC, Mo_2C/EPBC and Cu/EPBC catalysts. Fig. 4a displays the Mo 3d XPS in Cu-Mo_2C/EPBC and Mo_2C/EPBC catalysts, where three states (Mo^{2+}, Mo^{4+}, and Mo^{6+}) can be clearly observed after the peak deconvolutions of Mo_2C/EPBC sample [42, 43]. Notably, the Cu-Mo_2C/EPBC shows a larger content of Mo^{4+} species as a comparison with that of Mo_2C/EPBC sample, demonstrating that the existence of N anchored Cu-Mo_2C cluster interface can induce the interfacial electron reconstruction thereby providing more Cu-MoO_xC_y active species. The Cu LMM AES exhibits two peaks at ~ 568.3 eV and ~ 573.2 eV, assigning to Cu^0 and Cu^+ states (Fig. 4b). The existence of a larger Cu^+ species in Cu-Mo_2C/EPBC further confirms that there was a strong interaction between Cu and Mo_2C, and some of the electrons have transferred from the Cu to Mo_2C species, forming special MoO_xC_y-Cu^+/Cu^0 species [34]. To deeply assess the N anchored Mo_2C clusters' interaction in Cu-Mo_2C/EPBC, we carried out XAS measurements at the Mo *K*-edge and Cu *K*-edge. The Cu-Mo_2C/AC was also used as a comparative analysis. The fingerprint effect of X-ray absorption near edge structure (XANES) ascertains the valence state of the absorption atom. Fig. 4c shows Mo *K*-edge XANES spectra for Cu-Mo_2C/EPBC, Cu-Mo_2C/AC and corresponding standard samples. The Cu-Mo_2C/EPBC and Cu-Mo_2C/AC exhibit the absorption edge between that of Mo foil and MoO_3, implying that their medium oxidation state. The absorption edge of Cu-Mo_2C/EPBC is slightly higher energy than for the Cu-Mo_2C/AC, indicating that the valence state of Mo is slightly higher than that of Cu-Mo_2C/AC, which is consistent with the XPS results shown in Fig. 3e. This disparity in valence state of Mo might stem from the distinctive regulation effects by the Mo-N charge transfer and stronger clusters interaction in Cu-Mo_2C/EPBC [31]. Meanwhile, we then resorted to extended X-ray absorption fine structure (EXAFS) spectra to investigate the local structure. As illustrated in Fig. 4d, the Cu-Mo_2C/EPBC exhibits two peaks at ca. 1.47 Å and ca. 2.76 Å, which comes from Mo-C and Mo-Mo path, respectively. Notable, the increaser bond length of Mo-C bond confirms the electron-deficient states of the Mo species caused by more electrons transfer from Mo to C or N. Furthermore, as demonstrated by the XANES of Cu-Mo_2C/EPBC and Cu-Mo_2C/AC of Cu *K*-edge, the pre-edge centroids slightly shift to higher values compare with Cu-Mo_2C/AC, further implying that a stronger Cu-Mo_2C interaction of Cu-Mo_2C/EPBC compared to Cu-Mo_2C/AC (Fig. 4e). Obviously, the Mo_2C clusters with electron-deficient states induced by pyridinic N triggered the Cu atoms/clusters electron transfer, leading to Cu^+/Cu^0-Mo_2C active species [30]. Furthermore, the Cu *K*-edge FT-EXAFS spectra were depicted in Fig. 4f. The Cu-Mo_2C/EPBC and Cu-Mo_2C/AC demonstrate a predominant path at around 1.53 Å and a weak peak at 2.2 Å, corresponding to Cu-O and Cu-Cu

Journal Pre-proof

scattering path, respectively. A weaker peak of Cu-Cu band in Cu-Mo_2C/EPBC indicates that Mo_2C loaded on rich-N EPBC facilitate Cu atoms to homogeneous distribute on the surface of Mo_2C clusters in the form of clusters, rather than Cu-Mo_2C particles-particles interface in the case of AC. We further performed the wavelet transform (WT) EXAFS analysis to distinguish back-scattering atoms in the *k*-space (Fig. 4g-i). The WT-EXAFS of Cu-Mo_2C/EPBC shows the maximum intensity values at 4.8 and 10.0 $Å^{-1}$ corresponding to the Mo-C and Mo-Mo contributions, respectively. The above changes in valence states for Mo and Cu corroborate the stronger electronic interactions at the Cu-Mo_2C interfaces in Cu-Mo_2C/EPBC, and such interactions is considered sensitive for the size of the anchored metal active sties.

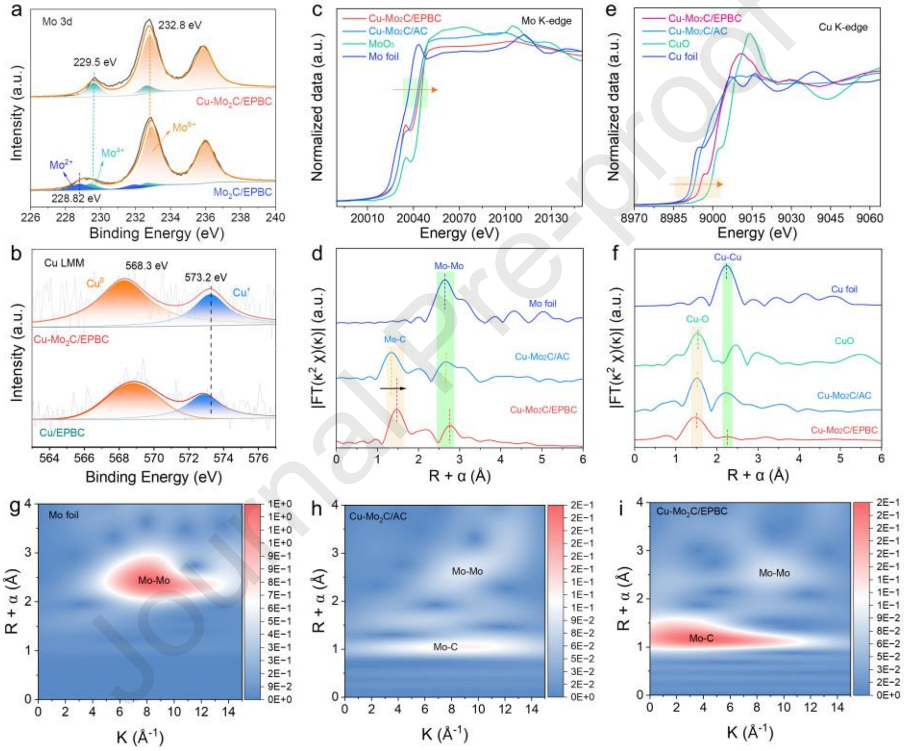

Fig. 4. (a) XPS spectra of Mo 3d in Cu-Mo_2C/EPBC and Mo_2C/EPBC; (b) Cu LMM AES of Cu-Mo_2C/EPBC and Cu/EPBC catalysts; (c) Mo *K*-edge XANES and corresponding standard samples; (d) Fourier-transformed k^2-weight EXAFS of Mo *K*-edge; (e) Cu *K*-edge XANES and corresponding standard samples; (f) Fourier-transformed k^2-weight EXAFS of Cu *K*-edge; (g-i) Mo *K*-edge WT-EXAFS spectra of Mo foil, Cu-Mo_2C/AC and Cu-Mo_2C/EPBC, respectively.

2.2. Catalytic performance of RWGS reaction

The catalytic performance of Cu-Mo_2C/EPBC and contrastive catalysts for RWGS reaction at low temperature was evaluated in a fixed-bed reactor (Fig. 5a). The catalytic activity of the Cu-Mo_2C/EPBC catalyst was first associated with the bimetal loading. As demonstrated by Fig. 5b, the

Journal Pre-proof

samples with 0.8 wt.% Cu loading showed optimal CO_2 conversion and CO selectivity when Mo_2C content in the Cu-Mo_2C/EPBC catalyst was fixed at 20 wt.%, suggesting that suitable Cu/Mo_2C ratio in Cu-Mo_2C/EPBC paly an importance role in the catalytic performance for RWGS reaction. Considering the synergistic effect between pyridine N anchoring and cluster interactions as the main reason for the good dispersion of metal active sites on the catalyst surface, it may lead to metal sintering that produces larger metal particles and weakens catalytic reactivity when Cu loading exceeds the threshold for synergistic effects [44]. Further, the threshold effect remains even when Mo_2C content in Cu-Mo_2C/EPBC was not fixed. As shown in Fig. 5c, the 1.0 wt.%Cu-25 wt.%Mo_2C/EPBC catalyst showed a slight decrease in the CO_2 conversion rate and CO selectivity than that of 0.8 wt.%Cu-20 wt.%Mo_2C/EPBC.

To experimentally demonstrate the positive contribution of the synergistic effects to RWGS reaction, the catalytic performance of Cu-Mo_2C/EPBC, Cu-Mo_2C/AC, Cu/EPBC and Mo_2C/EPBC were measured (Fig. 5d). It was discovered that Cu/EPBC has no clear catalytic performance, while the Mo_2C/EPBC shows better performance. The Cu-Mo_2C/EPBC displays an improved CO selectivity of 99.95% at 500 °C compared with Cu-Mo_2C/AC (99.60%), as well as about 3-fold CO_2 conversion rate per catalyst mass. Optimal catalytic performance even presents at lower reaction temperatures (400 °C and 450 °C). In addition, the Cu-Mo_2C/EPBC-850 and Cu-Mo_2C/EPBC-900 also exhibit much better catalytic performance than that of Cu-Mo_2C/AC (Fig. S15). The above results indicate that the synergistic effect between pyridinic N anchoring and the clusters contributes to excellent RWGS reaction performance of Cu-Mo_2C/EPBC, which may promote the hydrogenation of CO_2 species to form CO*+OH*+H* species and subsequently selective composition into CO and H_2O [45], matching with the low apparent activation energy (E_a) for Cu-Mo_2C/EPBC (Fig. 5e). Long-term evaluation of the Cu-Mo_2C/EPBC catalyst was conducted and displayed in Fig. 5f. It is demonstrated that this catalyst exhibits excellent stability and maintained more than 99% of its initial activity after 50 h test. Meanwhile, the CO selectivity remained stable over 99.95%. Importantly, the used Cu-Mo_2C/EPBC presents neither bimetal sintering nor change of metal valence state and binding energy after the stability test as revealed by the XRD, XPS, HRTEM results (Fig. S16-18), considering the potential deactivation mechanisms for the catalyst. Moreover, among the as-prepared and literature reported metal support catalysts, the reaction rate (based on the metal sites) of Cu-Mo_2C/EPBC was as high as 1354 $\mu mol_{CO2}/g_{metal}/s$ at 500 °C and very low H_2 partial pressure, which was at least two times higher than that of other reported non-noble metal-based and even noble metal-based catalysts (Fig. 5g and Table S6). These observations strongly confirm the synergistic effect between pyridine N anchoring and cluster interaction facilitates the realization of an excellent RWGS reaction [30].

Journal Pre-proof

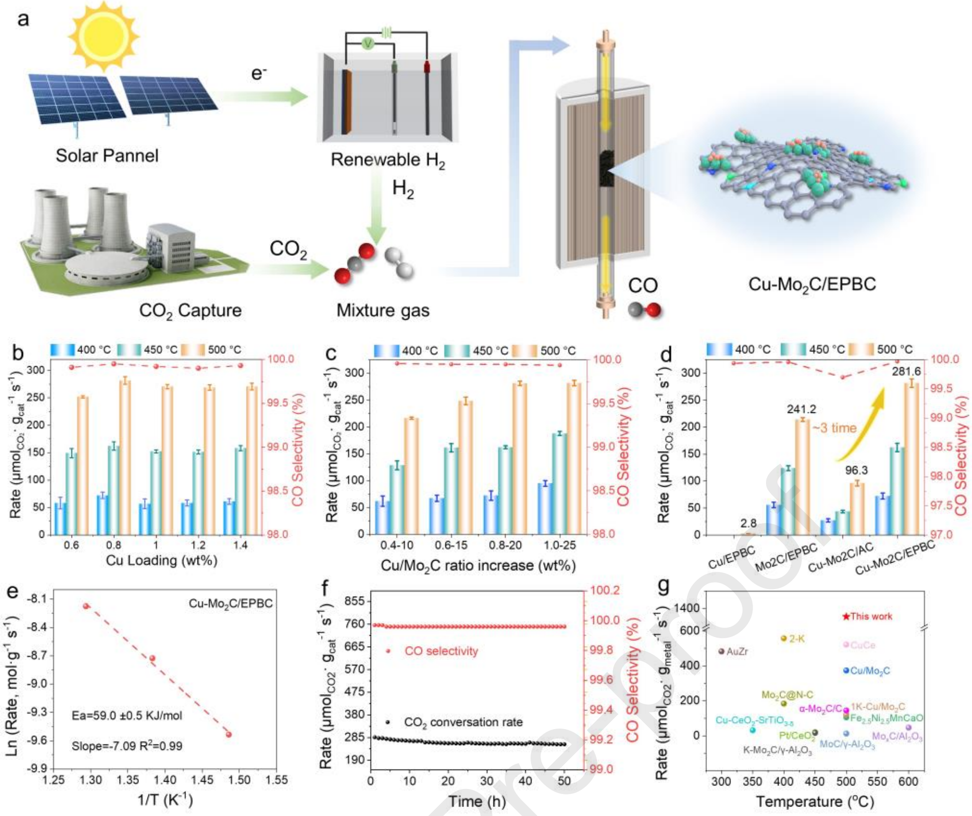

Fig. 5. (a) Schematic illustration of the thermal CO_2 hydrogenation to CO; (a,b) Conversion rate and CO selectivity over Cu-Mo_2C/EPBC with different Cu loading (b) and Cu-Mo_2C loading (c); (d) Catalytic performance between EPBC and AC supported catalysts; (e) Apparent activation energy (E_a) determined by Arrhenius plots based on CO_2 hydrogenation; (f) Catalytic stability of Cu-Mo_2C/EPBC; (g) Comparison of Cu-Mo_2C/EPBC with the reported RWGS catalysts. Reaction condition: atmospheric pressure, CO_2:H_2=1:2, T = 500 °C, GHSV=300000 ml/g/h for EPBC and AC supported catalysts; CO_2:H_2=1:2-1:3, T=350-500 °C, GHSV=13000-400000 ml/g/h for the others.

DFT calculations were performed to gain a better understanding of the electron transfer processes occurring at the interface between metal clusters (Cu-Mo_2C) and carbon or nitrogen doped carbon. Two models were built and optimized to simulate the structure of Cu-Mo_2C/AC and Cu-Mo_2C/EPBC, as shown in Fig. 6a-b. The charge density difference comparison reveals that the charge redistribution is localized in a limited region near the interface between metal particles and N or C site of support. Bader charge analysis predicts increased charge accumulation (+3.90 qe) between Cu-Mo_2C cluster and N site (Fig. 6a) compared to C site (+2.78 qe, Fig. 6b), indicating that the electron transfer from Cu-Mo2C to N site is enhanced compared to electron transfer from Cu-Mo_2C to C site. This indicates the doping of N effectively promotes the charge transfer between Cu/Mo_2C and carbon. To further prove the electronic interaction between pyridine N-modified carbon matrix and Cu-Mo_2C clusters

Journal Pre-proof

sites, the DFT calculations were also conducted to simulate the path of the mechanism on the Cu-Mo_2C/EPBC and Cu-Mo_2C/AC. Fig. 6c shows the energy profiles of CO formation via the redox pathways [46, 47]. The whole CO_2 conversion path on the interface of Cu-Mo_2C/EPBC and Cu-Mo_2C/AC remains energetically favorable, especially Cu-Mo_2C/EPBC. DFT calculations reveal that the adsorption of CO_2 and H_2 on the surface of Cu-Mo_2C/EPBC is energetically favorable firstly, with a negative free energy of −2.13 eV. Then, the adsorbed CO_2 dissociation into CO* and O* by overcoming a highest transition state barrier of 0.61eV which is the rate-limit step. While the rate-limit step of Cu-Mo_2C/AC model is CO*+O*+2H*, forming CO*+O*+H* with the transition state barrier of 1.52 eV. Therefore, the transition of the rate-limiting step and the decrease of the energy barrier over Cu-Mo_2C/EPBC benefits from the interaction between pyridine N and Cu-Mo_2C cluster interface, resulting a superior catalytic performance to the Cu-Mo_2C/AC [48]. This study provides a low-energy-consuming strategy for establishing nitrogen-doped carbon-based Cu-Mo_2C as efficient way for the application of a Cu-Mo_2C system for CO_2 utilization.

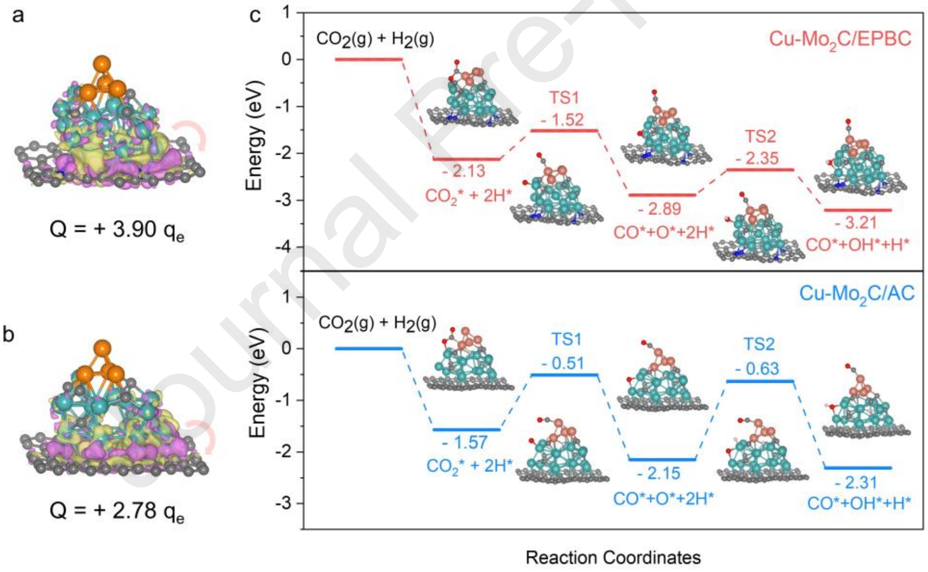

Fig. 6. (a,b) Charge density difference plots and Bader charge distributions for Cu-Mo_2C/EPBC (a) and Cu-Mo_2C/AC (b); (c) Calculated energy profile and intermediate structures for CO formation on Cu-Mo_2C/EPBC and Cu-Mo_2C/AC. The orange, green, black, red, and pink spheres represent Cu, Mo, C, O, and H, respectively.

3. Conclusion

In summary, we have developed a highly efficient and stable Cu-Mo_2C/EPBC catalyst via biomass-derived strategy for RWGS reaction. Experiments and DFT calculations show that a significant electron transfer occurs after nitrogen doping, that is, the synergistic effect between

Journal Pre-proof

pyridine N anchoring and cluster interaction in Cu-Mo_2C/EPBC improves the interfacial electronic structure, which regulates the size and distribution of metal clusters, exposes more active sites on the catalyst. Meanwhile, the mesoporous structure of EPBC enhances the dispersion of Cu-Mo_2C clusters and facilitates the CO_2 and H_2 adsorption and mass transfer. The constructed Cu-Mo_2C/EPBC displays an improved CO selectivity of 99.95% at 500 °C compared with Cu-Mo_2C/AC catalyst (99.60%), as well as about 3-fold CO_2 conversion rate. The theoretical calculations suggest that the synergistic catalysis arising from the Cu-Mo_2C location adjacent to N sites in EPBC enhances the adsorption of substrate molecules and reduces the energy barrier of reactants dissociation. This work can provide a new insight for the designing and fabricating high CO_2 conversion rate and CO-selective RWGS catalysts at low temperatures.

Journal Pre-proof

4. Experimental

4.1. Synthesis of catalysts

EP was cleaned and dried naturally after collection. The dried EP containing abundant cellulose and protein was directly carbonized at a target pyrolysis temperature (800, 850, and 900 ℃) for 2 h under N_2 atmosphere. The biochar product was continuously washed three times with 1 M HCl, and with DI water until the pH of the supernatant was neutral. After drying at 110 ℃ for an overnight period, the EP-derived biochar was obtained. For simplicity, the resultant sample is denoted as EPBC-T, where T stands the pyrolysis temperature. For comparison, the coconut shells derived AC was prepared by steam physical activation method according to our previous study [49].

Cu-Mo_2C/EPBC precursor was synthesized using the impregnation method. Typically, the aqueous solution of $(NH_4)_6Mo_7O_{24}\cdot 4H_2O$ and $Cu(NO_3)_2\cdot 3H_2O$ were employed with the calculated weight to obtain the target metal loading and mixed under stirring at room temperature, then prepared EPBC was immersed into the prepared mixture. This mixture was further impregnated at room temperature for 24 h and then dried at 80 °C for 12 h under vacuum. In order to determine the optimal Cu-Mo ratio, the Mo loadings was 20 wt.% in all cases, while Cu was loading by impregnation of different concentrations of $Cu(NO_3)_2$ (0.6-1.4 wt.%). Then the metal load was adjusted synchronously to obtain the optimal metal utilization rate. Subsequently, Cu-Mo_2C/EPBC catalysts were prepared by carbothermal hydrogen reduction method. The resultant samples were placed into a tube furnace under a 10% H_2/N_2 flow at 800 °C for 2 h. Finally, the sample was cooled down to room temperature and passivated in a O_2/N_2 mixture at 200 mL/min for 2 h.

In this way, the samples were prepared and labelled according to the metal loading amount: x%Cu-y%Mo_2C/EPBC (x and y represent the amount of loaded metal). The metal content of all characterized samples is 0.8 wt.%Cu-20 wt.%Mo_2C without special explanation. Otherwise, the Cu/EPBC and Mo_2C/EPBC were prepared with single metal Cu and Mo_2C with loads of 0.8 wt.% and 20 wt.%, respectively. Cu-Mo_2C/AC was synthesized by a method similar to that of Cu-Mo_2C/EPBC, except that AC was chose as a carbon material.

4.2. Physical characterization

The surface areas and pore volumes were measured on an ASAP 2460 (Micromeritics, America) volumetric adsorption apparatus at 77 K using liquid N_2. The catalyst was degassed under a vacuum at 150 °C for 10 h. Micropore volume (V_{micro}), mesopore volume (V_{meso}) and macropore volume (V_{macro}) were obtained according to the non-local density functional theory (NLDFT). The S_{BET} and pore volume (V_{total}) were obtained according to Brunauer-Emmett-Teller (BET) method and volume absorbed at $P/P_0=0.99$, respectively. XRD patterns were recorded on a Rigaku Ultima (Japan) using Cu Kα radiation at 40 kV. The 2θ range was between 20° and 80°, with a step of 5°/min. TEM images were recorded on a Tecnai G2 (FEI, America) microscope operating at 200 Kv. HAADF-STEM images were recorded on a ARM200F (JOEL, Japan) microscope. The Cu, Mo, N identification and relative distribution were mapped by EDS coupled with TEM. XPS analysis was performed over a K-Alpha spectrometer (Thermo Scientific, America), using Al Kα radiation as an excitation source and all binding energies were referenced to C 1s of 284.8 eV. The XAS measurements for the Cu K-edge and Mo K-edge were conducted at BL14W1 beamline station of Shanghai Synchrotron Radiation Facility (SSRF). X-ray absorption fine structure (XAFS) measurements at Cu K-edge and Mo K-edge were performed with the Si(311) double-crystals monochromater (SSRF, 3.5 GeV, 250 mA in maximum).

Journal Pre-proof

XAFS data were processed by Demeter and EXAFS data were fitted using least-squares refinment by Artemis. Wavelet transform (WT) of Cu K-edge and Mo K-edge EXAFS oscillations were implemented using hamaFortran [50].

CO_2-TPD was also recorded on AutoChem II 2920 chemical adsorption instrument (Micromeritics, America). 50 mg catalyst was placed in U-shaped quartz tube and purged with He for 1 h for 110 °C at 50 ml/min. After the catalyst was cooled to 50 °C, 10% CO_2/He mixture was vented for 1h to saturation, then He air flow was switched to purge for 1h to remove the weakly physically adsorbed CO_2 on the surface, and finally desorption was carried out at a temperature rise of 5 °C /min to 800 °C under He atmosphere.

4.3. Catalytic performance of CO_2 hydrogenation to CO

The catalyst performance was evaluated in a fixed-bed reactor. Catalyst (40-60 mesh) was loaded into a stainless-steel reaction tube with an inner diameter of 8mm. After in-situ reduction in hydrogen atmosphere, the temperature of catalyst bed was adjusted to control the flow rate of raw gas for reaction (CO_2:H_2=1:2). The gas products were heated at the outlet of the reactor and then entered SHIMADZU GC-2014C gas chromatograph for online analysis, with nitrogen as internal standard. The area normalization method was used for quantitative detection. The calculation formulas of CO_2 conversion rate, CO selectivity, and the reaction rate of CO_2 according to catalyst and metal are shown in below respectively. Each test point is subjected to three parallel measurements.

$$X_{\mathrm{CO_2}}(\%) = \frac{n_{\mathrm{CO_2,in}} - n_{\mathrm{CO_2,out}}}{n_{\mathrm{CO_2,in}}} \qquad (1)$$

$$S_{\mathrm{co}}(\%) = \frac{n_{\mathrm{CO,out}}}{n_{\mathrm{CO,out}} + n_{\mathrm{CH_4,out}}} \qquad (2)$$

$$\mathrm{Rate}_{\mathrm{catalyst-CO_2}} = \frac{F_{\mathrm{CO_2}} \times X_{\mathrm{CO_2}}}{m_{cat}} \qquad (3)$$

$$\mathrm{Rate}_{\mathrm{metal-CO_2}} = \frac{F_{\mathrm{CO_2}} \times X_{\mathrm{CO_2}}}{m_{\mathrm{metal}}} \qquad (4)$$

Where: $n_{\mathrm{CO,out}}$, is the flow rate of CO in the outlet reformate;

$n_{\mathrm{CO_2,out}}$, is the flow rate of CO_2 in the outlet reformate;

$n_{CH_4,out}$ is the flow rate of CH_4 in the outlet reformate;

$n_{CO_2,in}$ is the flow rate of CO_2 in the feed;

F_{CO_2} is the mole flow rate of CO_2;

m_{cat} is the mass of catalyst;and m_{metal} is the mass of metal.*4.4. DFT calculations*

The Vienna Ab initio Simulation Package (VASP) software was used for the DFT calculations [51]. The generalized gradient approximation in the form of Perdew-Burke-Ernzerh (PBE) for the exchange-correction potential and a cutoff energy of 500 eV for the plane-wave basis were adopted. To consider long-range van der Waals (vdW) interactions, Grimme's DFT-D3 method was employed. Cu_4 cluster (Table S3), $Mo_{16}C_8$ cluster from Mo_2C (100), and single layer 4×4 nitrogen modified graphite structures were employed with 15 Å vacuum space in the vacuum-direction to avoid image interactions. A Gaussian smearing of 0.05 eV to the orbital occupation was applied during the geometry optimization and for the total energy computations. The 2 × 2 × 1 Monkhorst-Pack k-meshes were used to sample the Brillouin zone for geometry relaxation, whereas a denser mesh of 11 × 11 × 1 used to calculate the electronic structures. In charge density difference map, the isovalue of the isosurfaces is 3.0×10^{-3} eÅ^{-3}, and yellow (cyan) represents the charge accumulation (deletion). The convergence criteria of structure optimization were chosen as the maximum force on each atom less than 0.03 eV/Å with an energy change less than 10^{-5} eV. To calculate the kinetic energy barrier of chemical reactions, the climbing image nudged elastic band (CI-NEB) method with 6 images was used to search for the transition states (vibrational frequencies were evaluated to confirm minima and transition states), in which all of the force components perpendicular to the tangent of the reaction path were relaxed to be less than 0.05 eV/Å [52].

The adsorption energies (Eads) were calculated as the follow:

$$E_{\mathrm{ads}} = E(\mathrm{gas/slab}) - E(\mathrm{gas}) - E(\mathrm{slab}) \qquad (5)$$

Where: E(gas/slab) is the energy of H_2 or CO_2 adsorption in the different surfaces; E(gas) and E(slab) are the energies of isolated reaction molecular and clean catalyst slab, respectively.

References

[1] M. Ahmadi Khoshooei, X. Wang, G. Vitale, F. Formalik, K.O. Kirlikovali, R.Q. Snurr, P. Pereira-Almao, O.K. Farha, An active, stable cubic molybdenum carbide catalyst for the high-temperature reverse water-gas shift reaction, Science 384

Journal Pre-proof

(2024) 540-546.

[2] Y. Jia, F. Li, K. Fan, L. Sun, Cu-based bimetallic electrocatalysts for CO_2 reduction, Adv. Powder Mater. 1 (2022) 100012.

[3] A. Kumar, P. Daw, D. Milstein, Homogeneous catalysis for sustainable energy: hydrogen and methanol economies, fuels from biomass, and related topics, Chem. Rev. 122 (2022) 385-441.

[4] Z. Tian, Y. Wang, X. Zhen, Z. Liu, The effect of methanol production and application in internal combustion engines on emissions in the context of carbon neutrality: a review, Fuel 320 (2022) 123902.

[5] Z. Zhang, X. Chen, J. Kang, Z. Yu, J. Tian, Z. Gong, A. Jia, R. You, K. Qian, S. He, B. Teng, Y. Cui, Y. Wang, W. Zhang, W. Huang, The active sites of Cu-ZnO catalysts for water gas shift and CO hydrogenation reactions, Nat. Commun. 12 (2021) 4331.

[6] C. Yin, Q. Li, J. Zheng, Y. Ni, H. Wu, A.-L. Kjøniksen, C. Liu, Y. Lei, Y. Zhang, Progress in regulating electronic structure strategies on Cu-based bimetallic catalysts for CO_2 reduction reaction, Adv. Powder Mater. 1 (2022) 100055.

[7] K. Elouarzaki, V. Kannan, V. Jose, H. Sabharwal, J. Lee, Recent trends, benchmarking, and challenges of electrochemical reduction of CO_2 by molecular catalysts, Adv. Energy Mater. 9 (2019).

[8] R. Lim, M. Xie, M. Sk, J. Lee, A. Fisher, X. Wang, K. Lim, A review on the electrochemical reduction of CO_2 in fuel cells, metal electrodes and molecular catalysts, Catal. Today 233 (2014) 169-180.

[9] X. Zhang, M. Zhang, Y. Deng, M. Xu, L. Artiglia, W. Wen, R. Gao, B. Chen, S. Yao, X. Zhang, M. Peng, J. Yan, A. Li, Z. Jiang, X. Gao, S. Cao, C. Yang, A.J. Kropf, J. Shi, J. Xie, M. Bi, J.A. van Bokhoven, Y.W. Li, X. Wen, M. Flytzani-Stephanopoulos, C. Shi, W. Zhou, D. Ma, A stable low-temperature H_2-production catalyst by crowding Pt on alpha-MoC, Nature 589 (2021) 396-401.

[10] W. Geng, H. Han, F. Liu, X. Liu, L. Xiao, W. Wu, N,P,S-codoped C@nano-Mo_2C as an efficient catalyst for high selective synthesis of methanol from CO_2 hydrogenation, J. CO_2 Util. 21 (2017) 64-71.

[11] K.P. Reddy, S. Dama, N.B. Mhamane, M.K. Ghosalya, T. Raja, C.V. Satyanarayana, C.S. Gopinath, Molybdenum carbide catalyst for the reduction of CO_2 to CO: surface science aspects by NAPPES and catalysis studies, Dalton Trans. 48 (2019) 12199-12209.

[12] Y. Xu, Y. Yang, M. Wu, X. Yang, X. Bie, S. Zhang, Q. Li, Y. Zhang, C. Zhang, R.E. Przekop, B. Sztorch, D. Brzakalski, H. Zhou, Review on using molybdenum carbides for the thermal catalysis of CO_2 hydrogenation to produce high-value-added chemicals and fuels, Acta Phys. Chim. Sin. 40 (2024) 2304003.

[13] J. Xu, X. Gong, R. Hu, Z.W. Liu, Z.T. Liu, Highly active K-promoted Cu/β-Mo_2C catalysts for reverse water gas shift reaction: effect of potassium, Mol. Catal. 516 (2021) 111954.

[14] S. Posada-Perez, P.J. Ramirez, J. Evans, F. Vines, P. Liu, F. Illas, J.A. Rodriguez, Highly active Au/δ-MoC and Cu/δ-MoC catalysts for the conversion of CO_2: the metal/C ratio as a key factor defining activity, selectivity, and stability, J. Am. Chem. Soc. 138 (2016) 8269-8278.

[15] M.S. Duyar, C. Tsai, J.L. Snider, J.A. Singh, A. Gallo, J.S. Yoo, A.J. Medford, F. Abild-Pedersen, F. Studt, J. Kibsgaard, S.F. Bent, J.K. Nørskov, T.F. Jaramillo, A highly active molybdenum phosphide catalyst for methanol synthesis from CO and CO_2, Angew.Chem. Int. Ed. 57 (2018) 15045-15050.

[16] F. Wang, J. Jiang, K. Wang, Q. Zhai, F. Long, P. Liu, J. Feng, H. Xia, J. Ye, J. Li, J. Xu, Hydrotreatment of lipid model for diesel-like alkane using nitrogen-doped mesoporous carbon-supported molybdenum carbide, Appl. Catal. B Environ. 242 (2019) 150-160.

[17] F. Wang, W. Zhang, J. Jiang, J. Xu, Q. Zhai, L. Wei, F. Long, C. Liu, P. Liu, W. Tan, D. He, Nitrogen-rich carbon-supported ultrafine MoC nanoparticles for the hydrotreatment of oleic acid into diesel-like hydrocarbons, Chem. Eng. J. 382 (2020) 122464.

[18] M. Zhou, X. Jiang, W. Kong, H. Li, F. Lu, X. Zhou, Y. Zhang, Synergistic effect of dual-doped carbon on Mo_2C nanocrystals facilitates alkaline hydrogen evolution, Nano-Micro Lett. 15 (2023) 166.

Journal Pre-proof

[19] Y. Liu, G. Yu, G.D. Li, Y. Sun, T. Asefa, W. Chen, X. Zou, Coupling Mo_2C with nitrogen-rich nanocarbon leads to efficient hydrogen-evolution electrocatalytic sites, Angew.Chem. Int. Ed. 54 (2015) 10752.

[20] Y. Yan, Z. Zhao, J. Zhao, W. Tang, W. Huang, J. Lee, Atomic-thin hexagonal CuCo nanocrystals with d-band tuning for CO_2 reduction, J. Mater. Chem. A. 9 (2021) 7496-7502.

[21] Y. Yan, Z. Zhao, J. Zhao, Y. Xu, Y. Xu, Y. Zhao, W. Tang, J. Lee, Ultrathin CuNi nanosheets for CO_2 reduction and O_2 reduction reaction in fuel cells, ACS Mater. Lett. 3 (2021) 1143-1150.

[22] H. Zhou, T. Liu, X. Zhao, Y. Zhao, H. Lv, S. Fang, X. Wang, F. Zhou, Q. Xu, J. Xu, C. Xiong, Z. Xue, K. Wang, W.-C. Cheong, W. Xi, L. Gu, T. Yao, S. Wei, X. Hong, J. Luo, Y. Li, Y. Wu, A supported nickel catalyst stabilized by a surface digging effect for efficient methane oxidation, Angew.Chem. Int. Ed. 58 (2019) 18388-18393.

[23] S. Jing, L. Zhang, L. Luo, J. Lu, S. Yin, P.K. Shen, P. Tsiakaras, N-doped porous molybdenum carbide nanobelts as efficient catalysts for hydrogen evolution reaction, Appl. Catal. B Environ. 224 (2018) 533-540.

[24] X. Hu, C. Zhao, X. Hu, Q. Guan, Y. Wang, W. Li, Nitrogen-doped carbon cages encapsulating CuZn alloy for enhanced CO_2 reduction, ACS Appl. Mater. Interfaces 11 (2019) 25100-25107.

[25] M. Ren, T. Zhang, Y. Wang, Z. Jia, J. Cai, A highly pyridinic N-doped carbon from macroalgae with multifunctional use toward CO_2 capture and electrochemical applications, J. Mater. Sci. 54 (2019) 1606-1615.

[26] Z. Li, X. Wu, X. Jiang, B. Shen, Z. Teng, D. Sun, G. Fu, Y. Tang, Surface carbon layer controllable Ni_3Fe particles confined in hierarchical N-doped carbon framework boosting oxygen evolution reaction, Adv. Powder Mater. 1 (2022) 100020.

[27] J. Chen, H. Li, C. Fan, Q. Meng, Y. Tang, X. Qiu, G. Fu, T. Ma, Dual single-atomic $Ni\text{-}N_4$ and $Fe\text{-}N_4$ sites constructing janus hollow graphene for selective oxygen electrocatalysis, Adv. Mat. 32 (2020) 2003134.

[28] S. Ning, M. Li, X. Wang, D. Zhang, B. Zhang, C. Wang, D. Sun, Y. Tang, H. Li, K. Sun, G. Fu, Importing antibonding-orbital occupancy through Pd–O–Gd bridge promotes electrocatalytic oxygen reduction, Angew.Chem. Int. Ed. 62 (2023) e202314565.

[29] C. Fan, X. Wang, X. Wu, Y. Chen, Z. Wang, M. Li, D. Sun, Y. Tang, G. Fu, Neodymium-evoked valence electronic modulation to balance reversible oxygen electrocatalysis, Adv. Energy Mater. 13 (2023) 2203244.

[30] M. Zheng, P. Li, G. Fu, Y. Chen, Y. Zhou, Y. Tang, T. Lu, Efficient anchorage of highly dispersed and ultrafine palladium nanoparticles on the water-soluble phosphonate functionalized multiwall carbon nanotubes, Appl. Catal. B Environ. 129 (2013) 394-402.

[31] D. Zhao, K. Sun, W.C. Cheong, L. Zheng, C. Zhang, S. Liu, X. Cao, K. Wu, Y. Pan, Z. Zhuang, B. Hu, D. Wang, Q. Peng, C. Chen, Y. Li, Synergistically interactive pyridinic-N–MoP sites: identified active centers for enhanced hydrogen evolution in alkaline solution, Angew.Chem. Int. Ed. 59 (2019) 8982-8990.

[32] S. Nagakura, M. Kikuchi, S. Oketani, Electron diffraction determination of ionization of carbon atom in beta-Mo_2C crystal, Acta Crystallogr 21 (1966) 1009-1010.

[33] M. Juneau, M. Vonglis, J. Hartvigsen, L. Frost, D. Bayerl, M. Dixit, G. Mpourmpakis, J.R. Morse, J.W. Baldwin, H.D. Willauer, M.D. Porosoff, Assessing the viability of K-Mo_2C for reverse water-gas shift scale-up: molecular to laboratory to pilot scale, Energy Environ. Sci. 13 (2020) 2524-2539.

[34] K. Xiong, G. Zhou, H. Zhang, Y. Shen, X. Zhang, Y. Zhang, J. Li, Bridging Mo_2C–C and highly dispersed copper by incorporating N-functional groups to greatly enhance the catalytic activity and durability for carbon dioxide hydrogenation, J. Mater. Chem. A. 6 (2018) 15510-15516.

[35] Du，Yuchan, Wang，Fei, Xia，Xueying, Zhu，Hao, Zhang，Zeng, You，Chaoqun, Jiang，Xiaoxiang, Jiang，Jianchun, Li，Changzhu, MOF-derived Co nanoparticle on nitrogen-rich carbon for fatty acid hydrotreatment into green diesel, Renew. Energy 198 (2022) 246–253.

[36] B. Li, X. Liu, A. Wang, C. Tan, K. Sun, L. Deng, M. Fan, J. Cui, J. Xue, J. Jiang, D. Yao, Biochar with inherited negative surface charges derived from Enteromorpha prolifera as a promising cathode material for capacitive deionization

Journal Pre-proof

technology, Desalination 539 (2022) 115955.

[37] A. Garcia, A. Nieto, M. Vila, M. Vallet-Regi, Easy synthesis of ordered mesoporous carbon containing nickel nanoparticles by a low temperature hydrothermal method, Carbon 51 (2013) 410-418.

[38] M. Chen, L.L. Shao, Y.P. Liu, T.Z. Ren, Z.Y. Yuan, Nitrogen-doped ordered cubic mesoporous carbons as metal-free counter electrodes for dye-sensitized solar cells, J. Power Sources 283 (2015) 305-313.

[39] H. Sun, Y. Zhang, C. Wang, M.A. Isaacs, A.I. Osman, Y. Wang, D. Rooney, Y. Wang, Z. Yan, C.M.A. Parlett, F. Wang, C. Wu, Integrated carbon capture and utilization: synergistic catalysis between highly dispersed Ni clusters and ceria oxygen vacancies, Chem. Eng. J. 437 (2022) 135394.

[40] X. Zhang, X. Zhu, L. Lin, S. Yao, M. Zhang, X. Liu, X. Wang, Y.W. Li, C. Shi, D. Ma, Highly dispersed copper over beta-Mo_2C as an efficient and stable catalyst for the reverse water gas shift (RWGS) reaction, ACS Catal. 7 (2017) 912-918.

[41] M. Figueras, R.A. Gutierrez, F. Vines, P.J. Ramirez, J.A. Rodriguez, F. Illas, Supported molybdenum carbide nanoparticles as an excellent catalyst for CO_2 hydrogenation, ACS Catal. 11 (2021) 9679-9687.

[42] Y. Huang, M. Li, F. Pan, Z. Zhu, H. Sun, Y. Tang, G. Fu, Plasma-induced Mo-doped Co_3O_4 with enriched oxygen vacancies for electrocatalytic oxygen evolution in water splitting, Carbon energy 5 (2023) e279.

[43] M. Li, X. Wang, H. Du, W. Dong, S. Ye, H. Liu, H. Sun, K. Huang, H. Li, Y. Tang, G. Fu, Oxophilic Tm-sites in MoS_2 trigger thermodynamic spontaneous water dissociation for enhanced hydrogen evolution, Adv. Energy Mater. 14 (2024) 2401716.

[44] R.Y. Chein, W.H. Chen, H. Chyuan Ong, P. Loke Show, Y. Singh, Analysis of methanol synthesis using CO_2 hydrogenation and syngas produced from biogas-based reforming processes, Chem. Eng. J. 426 (2021) 130835.

[45] J. Lu, S. Zhang, H. Zhou, C. Huang, L. Xia, X. Liu, H. Luo, H. Wang, Ir single atoms and clusters supported on α-MoC as catalysts for efficient hydrogenation of CO_2 to CO, Acta Phys. Chim. Sin. 39 (2023) 2302021.

[46] Y. Jiang, Y. Sung, C. Choi, G. Joo Bang, S. Hong, X. Tan, T.S. Wu, Y.L. Soo, P. Xiong, M. Meng-Jung Li, L. Hao, Y. Jung, Z. Sun, Single-atom molybdenum-N_3 sites for selective hydrogenation of CO_2 to CO, Angew.Chem. Int. Ed. 61 (2022) e202203836.

[47] H. Jing, Q. Li, J. Wang, D. Liu, K. Wu, Theoretical study of the reverse water gas shift reaction on copper modified β-Mo_2C(001) surfaces, J. Phys. Chem. C 123 (2019) 1235-1251.

[48] X. Sun, J. Yu, H. Zada, Y. Han, L. Zhang, H. Chen, W. Yin, J. Sun, Reaction-induced unsaturated Mo oxycarbides afford highly active CO_2 conversion catalysts, Nat. Chem. (2024). https://doi.org/10.1038/s41557-024-01628-4.

[49] H. Sun, M.Z. Ma, M.M. Fan, K. Sun, W. Xu, K. Wang, B.J. Li, J.C. Jiang, Controllable preparation of biomass derived mesoporous activated carbon supported nano-CaO catalysts for biodiesel production, Energy 261 (2022) 125369.

[50] H. Funke, M. Chukalina, A. Rossberg, Wavelet analysis of extended X-ray absorption fine structure data, Phys. Scr. T115 (2005) 232-234.

[51] J.P. Perdew, Y. Wang, Accurate and simple analytic representation of the electron-gas correletion-energy, Phys. Rev. B 45 (1992) 13244-13249.

[52] G. Henkelman, B. Uberuaga, H. Jónsson, A climbing image nudged elastic band method for finding saddle points and minimum energy paths, J. Chem. Phys. 113 (2000) 9901-9904.

Journal Pre-proof

Highlights

► *Enteromorpha prolifera*-derived mesoporous biochar supported Cu-Mo_2C catalyst was prepared.

► The existence of pyridine N in EPBC facilitates the formation of atomic-level Cu-Mo_2C clusters.

► Cu-Mo_2C/EPBC exhibits the high conversation rate for selective CO_2 hydrogenation to CO.

Journal Pre-proof